Physics of the Earth and Planetary Interiors 306 (2020) 106541

Contents lists available at ScienceDirect

Physics of the Earth and Planetary Interiors

journal homepage: www.elsevier.com/locate/pepi

The dimensions of scatterers in the lower mantle using USArray recordings of S-wave to P-wave conversions

Jeroen Ritsema[a],*, Satoshi Kaneshima[b], Samuel M. Haugland[a]

[a] Department of Earth and Environmental Sciences, University of Michigan, Ann Arbor, MI 48109, USA
[b] Department of Earth and Planetary Sciences, Kyushu University, Motooka, Nishi-ku, Fukuoka, Japan

ABSTRACT

Seismic recordings from the USArray of the October 1, 2013 Sea of Okhotsk earthquake and the May 24, 2010 Western Brazil earthquake include high-amplitude SxP signals due to S-wave to P-wave scattering about 150 to 200 km below the 660-km discontinuity below these events. The scattering structures have been mapped previously and interpreted as fragments of folded crust that subducted into the uppermost lower mantle. The USArray recordings are unique because SxP is visible at all stations of the USArray over a distance of 2000 km. The arrival times of SxP with respect to the P arrival times vary by 2–3 s across the USArray.

The 2–3 s arrival time variations of SxP suggest the finite dimensions of the scattering structures. We estimate the dimensions by beamforming waveforms for subsets of USArray stations and the uncertainty ranges by bootstrapping. In our analysis we assume that the high-frequency wave traveltimes can be modeled using ray theory and that wave-speed heterogeneity between the scattering point and the array does not affect SxP-P differential traveltimes. The results indicate that the scattering structures beneath the Sea of Okhotsk and western Brazil have dimensions of 20–160 km but the uncertainties are large. The variation of the SxP amplitude by a factor of two to three is likely due to the complex geometry of the folded crust. We attribute the down-and-up SxP waveform to the interference of S-wave to P-wave conversions at the top and bottom of a 10–20 km thick portion of the folded crust. Our results suggest that the subducted crust can retain thicknesses of 10–20 km even after being folded by subduction into the viscous lower mantle.

1. Introduction

Tomographic studies of the mantle based on the traveltimes and long-period waveforms of high-amplitude seismic phases have elucidated the seismic structure of Earth's mantle at scales larger than 100 to 1000 km. Mapping of small-scale heterogeneity relies on the modeling of high-frequency wave scattering. Stochastic analyses of PKP precursory signal have shown that scattering structures in the mantle have characteristic length scales of 1–10 km (e.g., Hedlin et al., 1997) and velocity contrasts with the ambient mantle of 0.1–0.3% (e.g., Margerin and Nolet, 2003). Array analyses of various body-wave phases have linked scattering in the lowermost mantle to remnants of subducted slabs (e.g., Cao and Romanowicz, 2007; Miller and Niu, 2008), ultra-low-velocity zones (e.g., Wen & Helmberger, 1998; Thomas et al., 2009; Vanacore et al., 2010), compositional heterogeneity (e.g., Frost et al., 2013), and CMB topography (e.g., Doornbos, 1978; Earle and Shearer, 1997; Mancinelli and Shearer, 2016). Scattering in the lower mantle has been associated with small-scale fragments of subducted basalt (e.g., Kaneshima and Helffrich, 1998; Rost et al., 2008; Kaneshima, 2016), or compositional heterogeneity in thermochemical piles (e.g., Schumacher et al., 2018).

There are several seismic probes for detecting small-scale heterogeneities in Earth's deep mantle that are invisible to tomography. These include ScS reverberations (e.g., Revenaugh and Jordan, 1991; Courtier and Revenaugh, 2008), P to S converted waves (e.g., Shen et al., 2003; Jenkins et al., 2017), PKPPKP precursors (e.g., Le Stunff et al., 1995; Frost et al., 2018), SS precursors (e.g., Waszek et al., 2018), P to P scattered waves (e.g., Rost et al., 2008; Schumacher et al., 2018), and S to P scattered waves (e.g., Kaneshima and Helffrich, 1998, 1999; Vanacore et al., 2006; He and Zheng, 2018). These complementary approaches are based on different scattering geometries and constrain scattering both globally and locally with different sensitivities to scales.

In this paper we analyze S to P scattered waves, which we abbreviate as SxP from hereon and describe in more detail in section 2. Numerous studies of SxP provide observational evidence of scattering below deep earthquakes in the upper half of the lower mantle (see the reviews by Kaneshima (2016) and Kaneshima (2019)). The dimensions and shapes of the scattering structures could help understand how slabs buckle and deform while crossing the mantle transition zone. Waveform analyses of SxP assuming horizontal (e.g., Niu et al., 2003) or tilted (e.g., Haugland et al., 2017) layers suggest that the scattering structures have a characteristic thickness of 10–20 km thick, as expected for fragments of subducted oceanic crust. The widths have been estimated by mapping scattering points for multiple earthquakes (e.g., Kaneshima & Helffrich, 1999; Kaneshima, 2009; Niu, 2014).

This paper contributes new observations of SxP produced by two

---

* Corresponding author.
E-mail address: jritsema@umich.edu (J. Ritsema).

https://doi.org/10.1016/j.pepi.2020.106541
Received 27 February 2020; Received in revised form 15 June 2020; Accepted 15 June 2020
Available online 17 June 2020

Table 1
Source parameters of events A and B and recorded SxP pulses.

	Region	Date	Lat (°N)	Lon (°E)	H (km)	M_W	SxP pulses	
A	Sea of Okhotsk	Oct 1, 2013	52.20	152.79	573	6.7	**A1** (32–34 s after P)	
B	Western Brazil	May 24, 2010	−8.11	−71.64	582	6.4	**B1** (21–22 s after P)	**B2** (39–41 s after P)

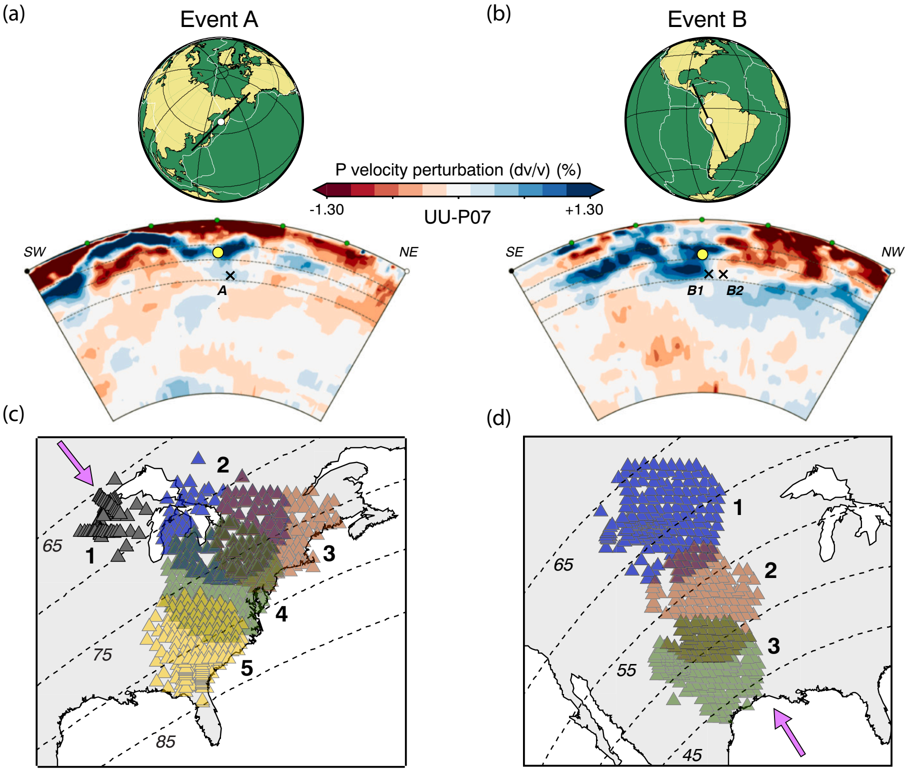

Fig. 1. The P-wave velocity structure according to tomographic model UU-P07 (Amaru, 2007) in 60°-wide cross-sections centered on the hypocenters (circles) of (a) event A and (b) event B. The images have been generated using SubMachine (Hosseini et al., 2018). The orientations of the cross sections are shown by black lines in the globes. The azimuths are 60° in (a) and 330° in (b). See also the purple arrows in (c) and (d). The crosses indicate approximately the locations of the scattering objects A, B1, and B2. The dashed lines are the 410-km and 660-km phase transitions and a horizon at 1000 km depth. (c and d) Locations of USArray stations in arrays, 1, 2, 3, 4, and 5 for event A (black, blue, brown, green, and yellow, respectively) and arrays 1, 2, and 3 for event B (blue, brown, and green, respectively). The dashed lines are equidistant from events A and B and have a spacing of 5°. The epicentral distance range is 65–85° for event A and 45–65° for event B. (For interpretation of the references to color in this figure legend, the reader is referred to the web version of this article.)

deep earthquakes beneath the Sea of Okhotsk and western Brazil and recorded by USArray stations distributed over a distance of about 2000 km. These observations are unique because, as discussed by Kaneshima (2018), most often SxP is modeled using arrays with a smaller aperture. The SxP arrival times vary by 2–3 s across the USArray which we attribute to scattering on different points on the same structures. As previous multiple-event studies we map the point scattering locations by beamforming and estimate how reliably we can estimate the dimensions of the scattering structures from analyzing of subsets of data. The accuracy is determined by the array geometry but not by the uncertainties in the event hypocenters and by differences in focal mechanisms. It is likely that the scattering structures are the same as those studied by Kaneshima (2009) using short-period data from the Pacific Northwest Seismic Network beneath the Sea of Okhotsk. This allows us to compare the dimensions of scattering structures estimated from multiple-event analysis of waveforms from the Pacific Northwest Seismic Network to our single-event analysis based on the USArray recordings.

2. Observations and methods

The seismic phase SxP is an S-wave to P-wave conversion at a scattering structure below the earthquake at depth x (e.g., Kaneshima, 2019). The conversion is relatively strong due to the large contrast between the velocities of the incident S wave and scattered P waves. In practice, deep earthquakes (> 400 km) produce the clearest SxP signals in the relatively quiet window between the P and the pP arrivals so SxP scattering studies are restricted to subduction zones. For small distance ranges, SxP arrives simultaneously with the outer core reflection PcP, but SxP and PcP can be distinguished easily as they have significantly different traveltime move-outs. The SxP scattering point is determined by the SxP-P traveltime difference. Its accuracy is limited primarily by the first Fresnel zone of about 100 km and the geometry of the array of seismometers.

2.1. The October 1, 2013 earthquake and the May 24, 2010 earthquake

We study recordings for the October 1, 2013 and the May 24, 2010 earthquakes. We refer to these earthquakes as events A and B and summarize the basic source parameters in Table 1. Fig. 1a and b shows the P-wave velocity variations according to model UU-P07 (Amaru, 2007) in vertical cross-sections through the event hypocenters. The cross-sections are directed towards the USArray stations that recorded events A and B, so they include the ray paths and the SxP scattering points. The scattering structures are located within or near high-velocity regions in UU-P07 and in other whole-mantle tomographic models (e.g., Hosseini et al., 2018).

At the time of event A in 2013, the USArray was deployed in the Great Lakes region and in states along the Atlantic Ocean. We divide the USArray into five circular arrays (Fig. 1c). Each subarray has a radius of about 500 km and includes more than 200 stations. Subarray 1 is the Superior Province Rifting Earthscope Experiment (Stein et al., 2011) west of Lake Michigan. Among the five subarrays, subarray 1 and has a relatively small diameter and the fewest number of stations which affects analytical precision. Subarrays 2, 3, 4, and 5 overlap. Subarray 2 includes USArray stations that were deployed in the Great Lakes region east of Lake Michigan. Subarrays 3, 4, and 5 include USArray stations along the Mid-Atlantic region of the United States from north to south.

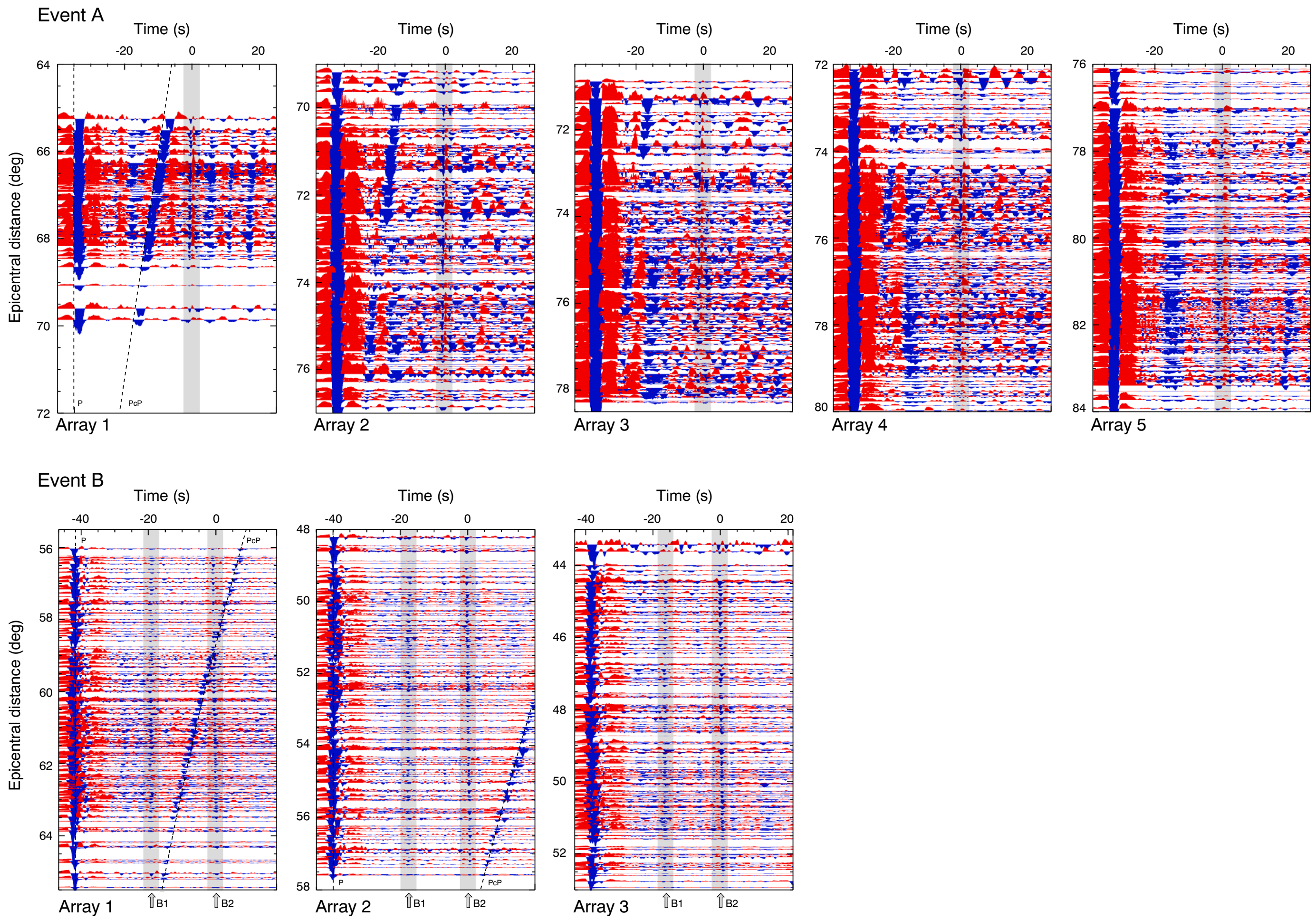

Fig. 2. Record section of displacement waveforms produced by (top row) event A and (bottom row) event B and recorded at stations from subarrays 1–5 (for event A) and 1–3 (for event B). The phase P is the earliest high-amplitude signal. The phase PcP is the second high-amplitude signal decreasing arrival time with respect to the P arrival time with increasing distance. The signals are aligned on the SxP phases (pulse B2 for event B) at arrival times t = 0. The SxP signals are indicated by grey rectangles. For event B, pulse B1 and pulse B2 arrive about 20 s and 40 s after P.

When event B occurred in 2010, the USArray was located in the central US (Fig. 1d). Subarrays 1, 2, and 3 with similar radii and number of stations as for event A are distributed from north to south across the central Great Plains of the United States.

Fig. 2 shows record sections of vertical component displacement waveforms for events A and B at all subarrays. The waveforms have been corrected for instrument responses to obtain recordings of ground displacement, bandpass filtered using a two-pass Butterworth filter with corner frequencies of 0.05 Hz and 4 Hz (i.e., periods shorter than 20 s), and aligned on the SxP signals. For event A, SxP arrives about 33 after P. From here on we call this SxP pulse A. Two SxP signals for event B are recorded at about 22 s and 40 s after the P wave arrival. We refer to these SxP phases as pulses B1 and B2, respectively. The recordings are aligned on pulse B2. Pulses B1 and B2 are also visible in broadband recordings from stations in Alaska albeit with lower quality.

The arrival times of pulses A, B1 and B2 after the P-wave arrival are listed in Table 1. Most likely, pulse A is the same as pulse K1 and that pulses B1 and B2 are the same as pulses P1 and P2 studied by Kaneshima (2009) using multiple events. He mapped the causative scattering structure of A below the Sea of Okhotsk at a depth of 920 ± 50 km and the two scattering structures beneath western Brazil associated with B1 and B2 at depths of 750 ± 50 km and 830 ± 90 km.

2.2. Beamforming and uncertainties

For each subarray we assume that pulses A, B1, and B2 are due to point scattering. To estimate the scattering points, we use a beamforming technique (see Rost and Thomas (2009) for a review of array processing techniques) following the original approach by Kaneshima and Helffrich (1998) and quantify the pulse alignment by semblance (e.g., Neidell and Taner, 1971; Kaneshima and Helffrich, 2010). Initially, we calculate the semblance for a 4-s wide window to search for SxP signals in the data. We pinpoint the scattering location by calculating the semblance for a fine grid of potential S-to-P scattering locations around the initial location and by reducing the time window for semblance analysis to 1 s.

Fig. 3 shows histograms of the SxP slowness with respect to the P-wave slowness (Δp) and azimuth deviations in clockwise sense from the back-azimuth direction (Δϕ). For the ranges of Δp and Δϕ in Fig. 3, the semblances are higher than 95% of the maximum values for each subarray and indicate therefore that the estimates of slowness and azimuth have substantial uncertainties. The slowness and azimuth ranges, summarized in Supplementary Table S1, depend on many factors such as the SxP pulse width, the signal quality, and the aperture and density of the network of stations that recorded SxP. For example, for event A, the uncertainty ranges of the slowness and azimuth of pulse

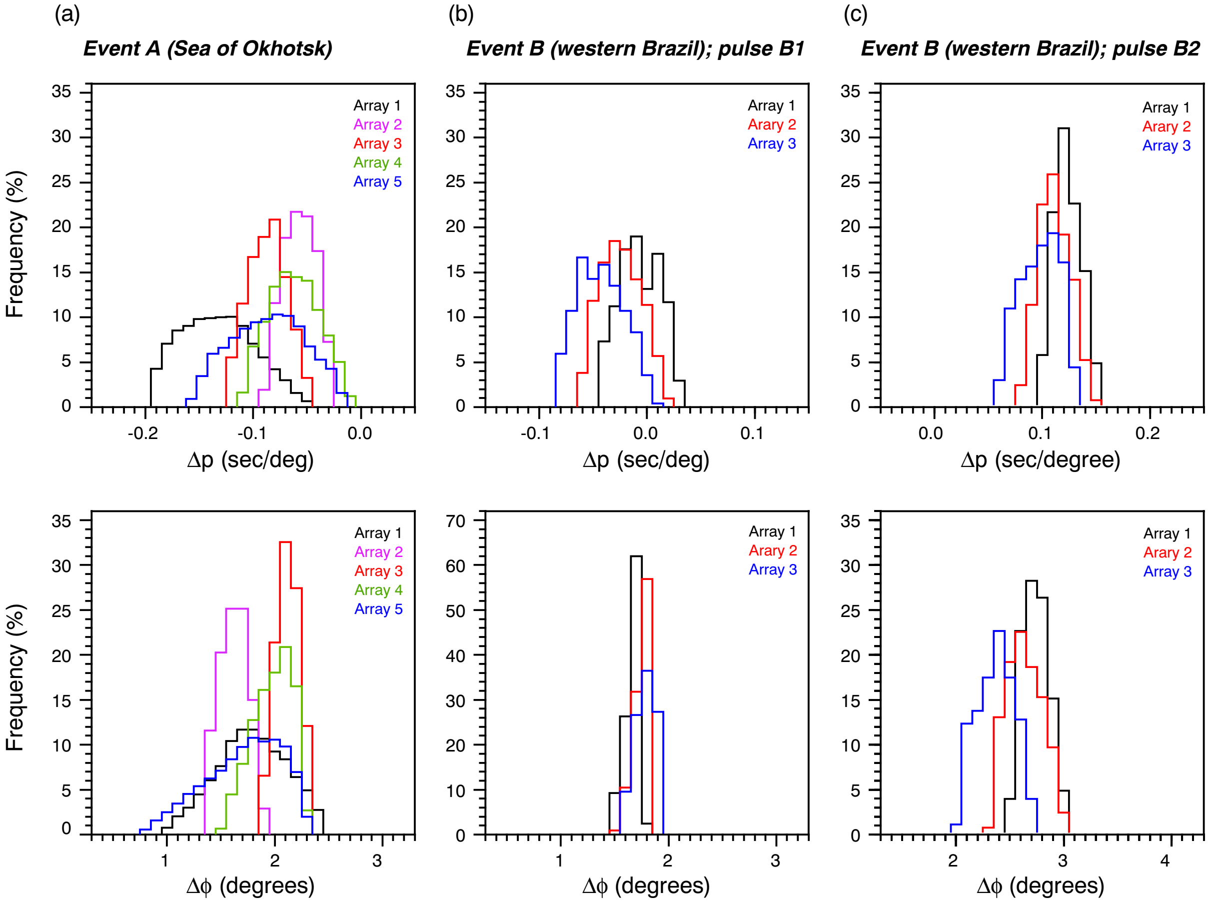

Fig. 3. Histograms of the (top) slowness and (bottom) arrival azimuth of SxP with respect to the P-wave for which the semblance is higher than 95% of the maximum value. (left) Event A (center and right) pulses B1 and B2 for event B.

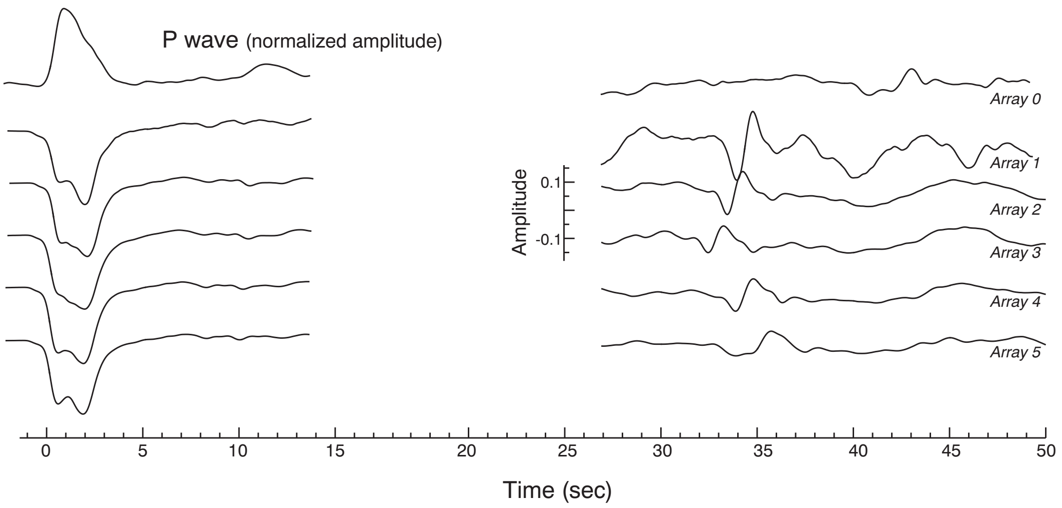

Fig. 4. The beam of displacement waveforms of (left) the P wave, scaled to have an amplitude of 1, and (right) the SxP signals recorded by (from top to bottom) arrays 1, 2, 3, 4, and 5 using a different vertical scale. The beam is not shown between 14 and 27 s after P.

A at subarrays 1 and 5 are wider than at subarrays 2, 3, and 4. The slowness and azimuth uncertainty ranges for pulses B1 and B2 are more uniform.

We find that pulses A, B1, and B2 arrive up to 1–3° off the back-azimuth direction. The slowness of pulse B2 is higher than the P-wave slowness. This indicates that the optimal scattering point lies outside the plane of wave propagation and that the S to P scattered waves are not formed by horizontally layered structures.

Using the arrival time, slowness, and arrival azimuth, we back-project pulses A, B1, and B2 from the center of the subarray to the S to P scattering points, assuming that the S-wave and P-wave segments of SxP are ray paths for the AK135 velocity structure (Kennett et al., 1995). Absolute scattering locations are uncertain due to velocity heterogeneity and uncertainties in the earthquake hypocenters. However, we expect that ray-theoretical modeling of arrival-time differences between P and SxP phases using AK135 predicted times is adequate for

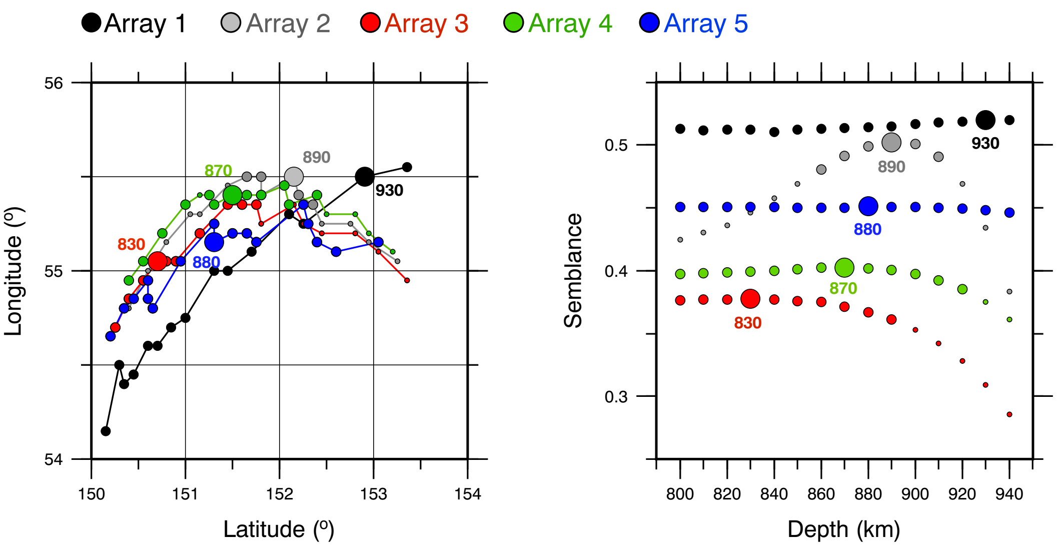

Fig. 5. (a) Scattering locations resolved for event A for assumed scattering depths from 800 km (lower left) to 960 km (upper right). Scattering locations have been resolved using a depth interval of 5 km but, for clarity, we show the locations for every 10 km. (b) Semblance as a function of scattering depth. In (a) and (b) the results for arrays 1, 2, 3, 4, and 5 are shown using black, grey, red, green, and blue circles and lines, respectively. The largest circles indicate the depths and locations where semblance is highest. The semblance is higher than 95% of the highest semblance for the locations and depths indicated by intermediate-size circles. (For interpretation of the references to color in this figure legend, the reader is referred to the web version of this article.)

estimating the relative scattering locations because SxP is a high-frequency signal and P and SxP phases propagate along nearly identical paths in the mantle from the scattering points to the receivers.

The uncertainties in the scattering locations are linked to the resolution of the slowness and back azimuth of the SxP phases. We quantify the uncertainty in the scattering locations from a bootstrapping analysis. For each subarray we generate 1000 random samples (sampling with replacement) of the waveforms and determine for each sample the scattering location (latitude, longitude, and depth) with highest semblance. The uncertainty in the distance between the scattering locations determined for two subarrays is determined by the median value and the range of distances between the one million locations pairs.

3. Analysis

3.1. Event A: October 1, 2013 Sea of Okhotsk

Fig. 4 shows stacks of the P waveform and pulse A for the five subarrays of the USArray that recorded event A. The five stacks are formed for the scattering locations that produce the highest semblance. Whereas the P-wave has a negative polarity as expected for the focal mechanism of event A, pulse A has an "down-and-up" waveform at all five arrays. Haugland et al. (2017) observed a similar waveform of S to P scattered waves for the 21 July 2007 western Brazil earthquake. They attributed this velocity-like waveform in the displacement ground-motion recording to interference of S-to-P conversions formed at the entry and exit points of an elongated and relatively thin scattering structure. The amplitude of pulse A is about 10% of the P wave amplitude and varies by about a factor of two. This indicates that the S to P scattering at each of the scattering points is not equally strong, presumably because the scattering structure has a complex shape. Pulse A is recorded between about 32 s (for array 3) and 34 s (for array 5) after the P wave. In addition to the predictable distance effects, this two-second arrival time variation of pulse A indicates that SxP scattering points are different for the five subarrays.

The uncertainties in the estimates of the slowness and azimuth of pulse A (Fig. 3) translate to significant uncertainties in the estimates of the scattering locations. There is trade-off between the estimated location and depth of the scattering point because the shapes of the semblance maxima and the SxP isochrons are analogous. Fig. 5a shows the scattering locations as a function of assumed scattering depth for subarrays 1, 2, 3, 4, and 5. The scattering point for subarray 2 is estimated with highest precision. The semblance maximum of 0.50 is resolved for a scattering depth of 890 km and at 55.5°N and 152.2°E. For depths between 860 km and 915 km, the semblance is smaller by 10%. For subarrays 3 and 4, the optimal scattering depths are 830 km and 870 km with uncertainty intervals of 800–890 km and 800–920 km, respectively. For subarrays 1 and 5, the depth of the scattering points is uncertain for the 800 km to 940 km depth range explored in the analysis because semblance values are higher than 95% of the corresponding maxima. Supplementary Fig. S1 shows resolution of the slownesses and azimuths of pulses B1 and B2 event B.

The semblance maxima for subarrays 2 and 4 overlap so it is uncertain whether these subarrays detect different scattering points. Despite the relatively poor resolution of the scattering locations for subarrays 1 and 5 their isochron are about 50 km south of the isochrons for subarrays 2, 3, and 4 so the scattering points beneath the Sea of Okhotsk associated with pulse A recorded by subarrays 1 and 5 are likely different than the scattering locations estimated for the other subarrays.

We quantify the uncertainties in the locations of scattering points using the bootstrapping procedure described in section 2.2. Fig. 6a shows the scattering points for subarrays 1, 2, and 4. To avoid clutter, we do not plot scattering locations for subarrays 3 and 5. The population of scattering locations for array 1 is wider than for arrays 2 and 4, consistent with the relatively broad semblance maximum for array 1 (Fig. 5). The scattering locations of arrays 2 and 4 overlap near the northwestern margin of the scattering locations of array 1, but they are at larger depths than the scattering points for array 1 in this region.

Fig. 6b, c and d shows cumulative frequency histograms of all 1000,000 distances between the scattering points determined for the 1000 bootstrap samples from arrays 1 and 2, 1 and 4, and 2 and 4. Supplementary Fig. S2 shows histograms of the scattering-point distances for all five arrays. The median distance of 40 km between the scattering points determined for arrays 2 and 4 is smaller than the median distance for any other pair of arrays for pulse A and 95% of the distances fall in the range 10–70 km. The 95% uncertainty interval

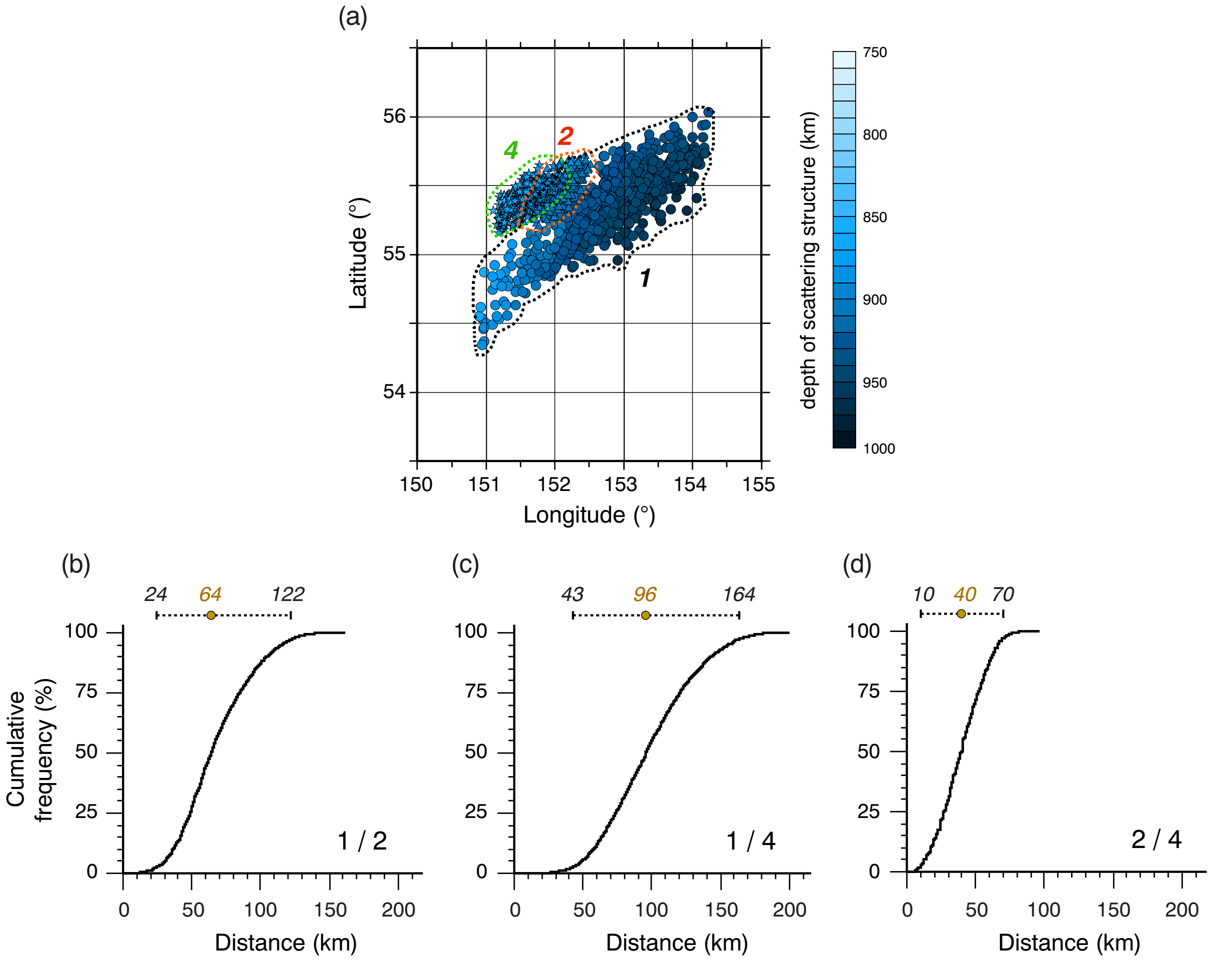

Fig. 6. (a) Locations of the scattering points for arrays 1 (circles), 2 (triangles), and 4 (stars) determined by bootstrap analysis. The symbol colors indicate the depths of the scattering points. The dashed lines (black for array 1; red for array 2; green for array 4) encircle the locations to clarify their horizontal spreads. (b, c and d) Cumulative frequency histograms of the distances between the scattering points of arrays 1 and 2 (in b), arrays 1 and 4 (in c), and arrays 2 and 4 (in d) determined by bootstrap analysis (see a). The brown circles and the horizontal bars indicate the median distances and the ranges that include 95% of all scattering-point distances (64 km and 24–122 km in b; 96 km and 43–164 km in c; 40 km and 10–70 km in d). (For interpretation of the references to color in this figure legend, the reader is referred to the web version of this article.)

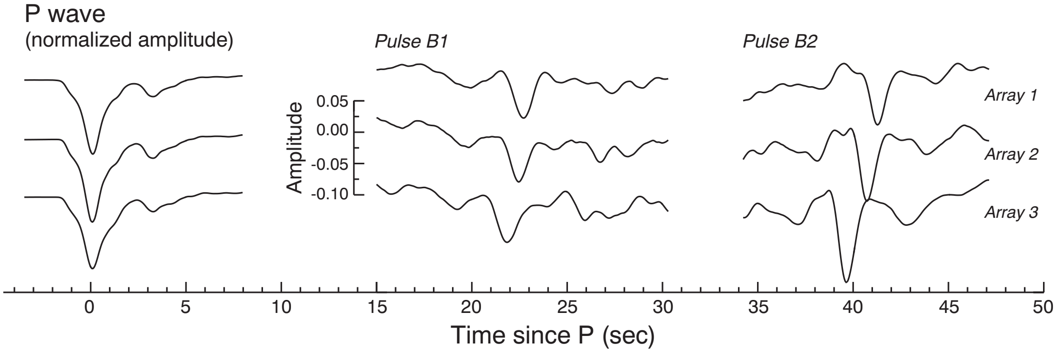

Fig. 7. The beam of displacement waveforms of (left) the P wave, scaled to have an amplitude of 1, and (right) two SxP signals (pulses 1 and 2) recorded by (from top to bottom) arrays 1, 2, and 3 using a different vertical scale for pulses B1 and B2. The SxP waveforms for each array have been time-shifted based on the arrival azimuth and slowness relative to P for which the semblance is highest. See also Fig. 5.

excludes 0 km but since modeling simplifications are not considered in the bootstrapping analysis, we cannot rule out that the scattering locations for arrays 2 and 4 are identical.

The median distances between scattering points resolved by arrays 1 and 2 and between arrays 1 and 4 are 64 km and 96 km, respectively. Their 95% confidence intervals of 24–122 km and 43–164 km respectively, are large because the scattering points for array 1 are distributed widely. Despite the large uncertainties, the scattering point for array 1

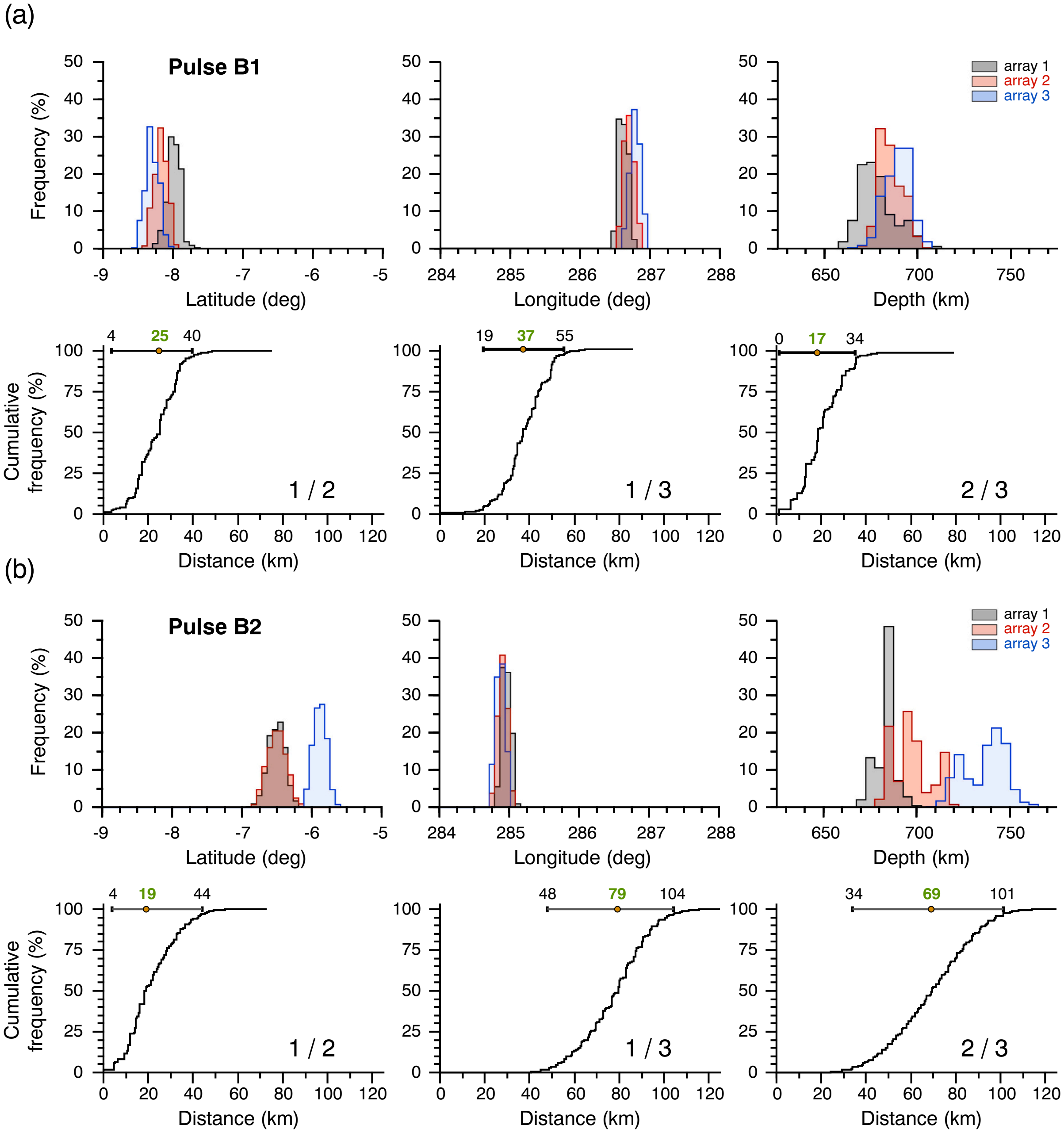

Fig. 8. Bootstrap analysis of (a) pulse 1 and (b) pulse 2 of event B. The top panels show histograms of the bootstrap locations of scattering points: latitude (left), longitude (middle), and depth (right). The bottom panels show cumulative frequency histograms of the distances between the scattering points of arrays 1 and 2 (left), 1 and 3 (middle), and 2 and 3 (right) determined by bootstrap analysis. The brown circles and the horizontal bars indicate the median distances and the ranges that include 95% of all scattering-point distances. (For interpretation of the references to color in this figure legend, the reader is referred to the web version of this article.)

is several tens to more than a hundred kilometers from the scattering locations for arrays 2 and 4. We find similar results for other arrays pairs for event A.

3.2. *Event B: May 24, 2010 Western Brazil*

Recordings of event B feature two SxP signals: B1 and B2. The two scattering structures that produced pulses B1 and B2 are 300 km apart. Pulse B2 formed to the northwest of pulse B1 and at slightly larger depth. Pulse B2 has the same amplitude as pulse A but pulse B1 is slightly weaker. The waveforms of B1 and B2 have a small upward first motion and not the large upward motion following the downward motion that characterizes pulse A. This may indicate that the scattering structure responsible for pulses B1 and B2 is rounder than the more layered structure that produced the down-and-up shape of pulse A.

Like pulse A for event A, the arrival times of pulses B1 and B2 vary by several seconds across stations of the USArray. In the beams for subarrays 1, 2, and 3 shown in Fig. 7, pulse B1 arrives about 21–22 s after the direct P wave. Pulse B2 is recorded with a larger variation. The arrival time is 39 s for subarray 3, 40 s for subarray 2, and 41 s for subarray 1. The different arrival times of B1 and B2 indicate that the scattering points on the scattering structures at subarrays 1, 2 and 3 differ by several tens of kilometers.

We use the same beamforming of pulses B1 and B2 and the bootstrapping analysis to estimate the locations and uncertainties of the scattering points as applied to event A. Fig. 8a and b shows the results

Table 2
Median distances (in km) and, in parentheses, the 95% confidence intervals between the scattering locations determined for groups 1, 2, 3, 4, and 5 for Event A and groups 1, 2, and 3 and pulse 1 and 2 of Event B. See also Supplementary Fig. S2.

Array	Event A			
	2	3	4	5
1	**64** (24–122)	**160** (56–282)	**96** (43–164)	**116** (24–230)
2		**105** (22 – 201)	**40** (10–70)	**62** (12–151)
3			**69** (11–174)	**68** (11–189)
4				**57** (11–126)

Array	Event B			
	Pulse B1		*Pulse B2*	
	2	3	2	3
1	**25** (4–40)	**37** (19–55)	**19** (4–122)	**79** (48–104)
2		**17** (0–34)		**69** (34–101)

of this analysis for pulses B1 and B2, respectively. The scattering points for pulse B1 are mapped progressively further to the south and at slightly larger depths at subarrays 1, 2 and 3. The median distance between the scattering points for subarrays 1 and 2 and for subarrays 2 and 3 is 25 and 17 km, respectively. The median distance between the scattering points determined for subarrays 1 and 3 is twice as large at 37 km. The 95% uncertainty interval of 19–55 km indicates that this separation of several tens of kilometers is well resolved. For pulse B2, the median distance of 19 km (with a 95% confidence interval of 4–44 km) between the scattering points for subarrays 1 and 2 reflects primarily the difference in the scattering depths. Pulse B2 recorded at subarray 2 is generated at a slightly larger depth than B2 recorded by subarray 1. In contrast, the scattering location of pulse B2 recorded by subarray 3 is to the north and at larger depths than the scattering points determined for subarrays 1 and 2. The median distances are 79 km and 69 km, respectively.

4. Discussion and conclusions

It has been a challenging task to estimate the size of heterogeneities in the lower mantle. Although stochastic studies of high-frequency PKP scattering indicates that scatterers have a characteristic length scale of 10 km, the assumption of wave propagation through randomly heterogeneous media seems inadequate to apply to the observations we present in this study. High-amplitude S to P scattering signals offer particularly high spatial resolution of the scattering structure because the Fresnel zone of about 100 km is relatively narrow and the SxP-P traveltime is not strongly affected by the effects of lateral heterogeneity (see Kaneshima, 2016, 2019 for reviews).

Recordings from the USArray of the October 1, 2013 Sea of Okhotsk earthquake (event A) and the May 24, 2010 Western Brazil earthquake (event B) include high-quality signals of S to P wave scattering – pulses A, B1, and B2 – in the uppermost lower mantle near 700–900 km depth. The scattering structures that produced pulses A, B1, and B2 are likely the same structures as K1, P1 and P2, respectively, mapped by Kaneshima (2009). Kaneshima (2009) estimated that scattering points for clusters of deep earthquakes in the vicinity of the hypocenters of events A and B vary by 200 to 300 km and pointed out that the inferred dimension of the scattering is uncertain because of uncertainties in the hypocenter locations and differences in event magnitudes, source durations, and focal mechanisms. The recordings of events A and B are unique in that the signals of S to P scattering are visible across the full extent of the USArray and may provide a better constraint on the dimensions of the scattering structures.

Pulse A, B1, and B2 have down-and-up waveshapes which we interpret as due to the interference of S to P converted waves at the entry and exit points of a 10–20 km think layer, as has been argued previously (e.g., Niu et al., 2003, Haugland et al., 2017). We constrain the widths of the scattering structures by beamforming recordings from three (for event B) and five (for event A) subsets of USArray stations. Although the absolute scattering points remain uncertain, the relatively locations of the scattering points for different subarrays are not sensitive to a mis-located hypocenter. Unless strong P-wave gradient exist, the relative locations are also not strongly affected by wave speed heterogeneity between the scattering points and the arrays because the beamforming is based on traveltime difference between SxP and P phases whose paths are nearly identical.

The 2–3 s variation in the arrival times of pulses A, B1, and B2 is consistent with scattering at different points that are separated by about 20 to 160 km. Table 2 shows a matrix of the distances between the scattering points inferred for the subarrays that recorded events A and B. A bootstrapping analysis indicates that the 95% confidence intervals are wide. The large uncertainties are inherent to the analysis primarily because the slowness and azimuth resolution is limited by the diameters (i.e., 500 km) of the subarrays and shear-velocity heterogeneity in the mantle between the earthquake and the scattering locations may cause small traveltime variations. In addition, our ray-theoretical analysis does not account for diffraction effects if the scattering structure has dimensions on the order of the size of the first Fresnel zone (i.e., about 100 km). Exploring these effects with 3-D synthetics is still impractical at high frequencies for a large number of scattering structures with

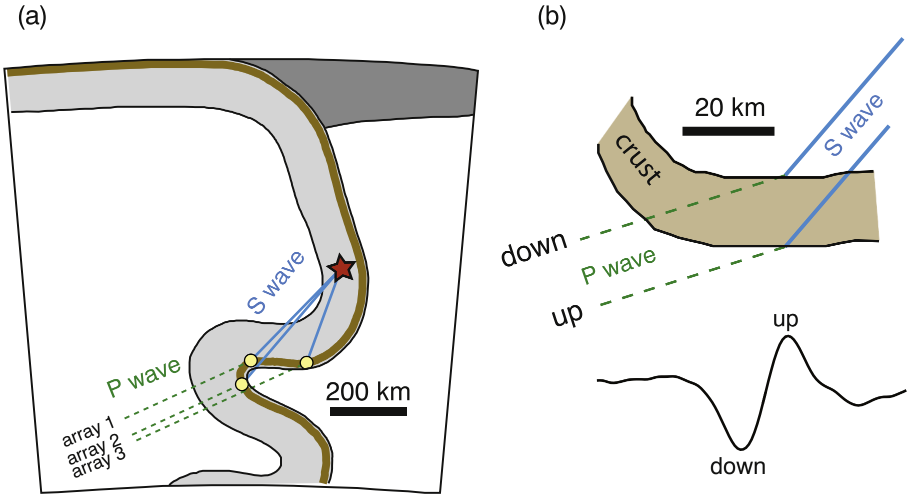

Fig. 9. Cartoon, based on Arredondo and Billen (2017), of the possible geometry of the scattering structure responsible for the recorded SxP signals. (a) Buckling of the slab in the uppermost lower mantle. The SxP signals are formed by S-wave to P-wave conversions in the uppermost lower mantle below the earthquakes (stars) at locations (yellow circles) on the folded crust. The different scattering points results in different SxP arrival times at different subset of USArray stations. (b) The down-up shape of the SxP ground displacement waveform is produced by the interference of two SxP conversions at the upper and lower boundaries of the crust. (For interpretation of the references to color in this figure legend, the reader is referred to the web version of this article.)

different shapes and dimensions although computational tools are becoming available for this purpose (Leng et al., 2019).

Despite large uncertainties, our analysis confirms previous inferences that the scattering structures are remnants of subducted basaltic crust (e.g., Kaneshima and Helffrich, 1999, 2009; Niu et al., 2003) that are relative thin ($<$ 10–20 km) and up to 100-km wide. Kaneshima (2009) pointed out that most scattering structures in the uppermost lower mantle are located near the bottom boundary of subducting slabs and therefore unlikely related to recently subducted oceanic crust. However, the resolution of seismic images of the uppermost mantle are not sufficiently high to resolve the complex shape of slabs that have crossed the 660-km boundary. Layers of crust may have been relocated if the slab buckled or overturned. If crust has peeled off from the slab, fragments may not immediately sink into the lower mantle because basalt-enriched rock has a lower density than the ambient mantle between the 660-km phase transition and about 750 km depth (e.g., Nakagawa et al., 2012).

Fig. 9a illustrates how the 100-km scattering structures may have produced scattering pulses A, B1, and B2 of events A and B. Our rendition of the slab is based on the simulations by Arredondo and Billen (2017) and the assumptions that the slab is overturned. The scattering structures are part of the crust still attached to the recently subducted slabs. The scattering points are separated by 50 to 200 km on this layer of crust based on our beamforming of subsets of USArray waveforms. The polarity, amplitude, and pulse width constrain the shear-wave contrasts and dimensions of the scattering structures (e.g., Kaneshima and Helffrich, 1999; Niu et al., 2003; Niu, 2014; Haugland et al., 2017). The nearly symmetric down-and-up shape of pulse A for event A beneath the Sea of Okhotsk suggests that the planar scattering structure is orthogonal to the S-wave propagation segment (Fig. 9b). Haugland et al. (2017) observed a similar waveshape in recordings of the 21 July 2007 western Brazil earthquake and showed using finite-difference seismograms that it can be explained by interference of wave conversions with opposite polarities at sharp sides of a 10–20 km thick layer with a shear velocity that is up to 10% lower than the shear velocity in the ambient mantle. The variation of the amplitude of pulse A by a factor of two is possibly due to a change in the angle between the surface of the scattering structure and the incident S wave.

Pulse B1 and B2 for event B in western Brazil are about 20 s apart. This arrival-time difference translates to a distance between two scattering structures of about 300 km. The arrival time variation across the USArray of pulse B1 is a second smaller than for pulse B2, which indicate that the scattering structure is more compact. Pulses B1 and B2 are more asymmetric than pulse A. This may imply that the crustal fragments are rounder or, if they planar scattering structures, the scattered wave paths have shallower refraction angles. A more quantitative analysis of the geometry of the scattering structures and the shear-velocity decrease within the crustal layer requires simulations of 3-D waveforms.

Data availability

Data from the TA network were made freely available as part of the EarthScope USArray facility, operated by Incorporated Research Institutions for Seismology (IRIS) and supported by the National Science Foundation, under Cooperative Agreements EAR-1261681. IRIS Data Services are funded through the Seismological Facilities for the Advancement of Geoscience (SAGE) Award of the National Science Foundation under Cooperative Support Agreement EAR-1851048. We thank Daniel Frost and an anonymous reviewer for constructive evaluations and Editor Vernon Cormier for overseeing the review process.

Funding

JR was supported by the National Science Foundation (EAR-1644829). SK was supported by MEXT/JSPS Kakenhi grant no. 15H05832 and 18K03784. SMH acknowledges support from University of Michigan fellowships.

CRediT authorship contribution statement

Jeroen Ritsema:Conceptualization, Methodology, Supervision, Software, Writing - original draft.**Satoshi Kaneshima**:Conceptualization, Methodology, Supervision, Software, Writing - original draft.**Samuel M. Haugland**:Visualization, Investigation, Software.

Declaration of competing interest

The authors declare that they have no known competing financial interests or personal relationships that could have appeared to influence the work reported in this paper.

Appendix A. Supplementary data

Supplementary data to this article can be found online at https://doi.org/10.1016/j.pepi.2020.106541.

References

Amaru, M., 2007. Global travel time tomography with 3-D reference models. Ph.D. thesis. Utrecht Univ., Utrecht, Netherlands.

Arredondo, K.M., Billen, M.I., 2017. Coupled effects of phase transitions and rheology in 2-D dynamical models of subduction. J. Geophys. Res. 122, 5813–5830. https://doi.org/10.1002/2017JB014374.

Cao, A., Romanowicz, B., 2007. Locating scatterers in the mantle using array analysis of PKP precursors from an earthquake doublet. Earth Planet. Sci. Lett. 255, 22–31.

Courtier, A.M., Revenaugh, J., 2008. Slabs and shear wave reflectors in the mid mantle. J. Geophys. Res. 113, B08312. https://doi.org/10.1029/2007JB005261.

Doornbos, D.J., 1978. On seismic-wave scattering by a rough core-mantle boundary. Geophys. J. R. Astron. Soc. 53, 643–662.

Earle, P., Shearer, P., 1997. Observations of PKKP precursors used to estimate small-scale topography on the core-mantle boundary. Science 277, 667–672.

Frost, D.A., Rost, S., Selby, N.D., Stuart, G.W., 2013. Detection of a tall ridge at the core–mantle boundary from scattered PKP energy. Geophys. J. Int. 195 (1), 558–574. https://doi.org/10.1093/gji/ggt242.

Frost, D.A., Garnero, E.J., Rost, S., 2018. Dynamical links between small- and large-scale mantle heterogeneity: seismological evidence. Earth Planet. Sci. Lett. 482, 135–146. https://doi.org/10.1016/j.epsl.2017.10.058.

Haugland, S.M., Ritsema, J., Kaneshima, S., Thorne, M.S., 2017. Estimate of the rigidity of eclogite in the lower mantle from waveform modeling of broadband *S*-to-*P* wave conversions. Geophys. Res. Lett. 44 (11), 778–11,784.

He, X., and Zheng, Y., S-to-P conversions from mid-mantle slow scatterers in slab regions: observations of deep/stagnated oceanic crust? *Pure Appl. Geophys.* 175, 2045–2055, https://doi.org/https://doi.org/10.1007/s00024-017-1763-z, 2018.

Hedlin, M.A.H., Shearer, P., Earle, P.S., 1997. Seismic evidence for small-scale heterogeneity throughout the Earth's mantle. Nature 387, 145–150.

Hosseini, K., Matthews, K.J., Sigloch, K., Shephard, G.E., Domeier, M., Tsekhmistrenko, M., 2018. SubMachine: web-based tools for exploring seismic tomography and other models of Earth's deep interior. Geochem. Geophys. Geosys. 19. https://doi.org/10.1029/2018GC007431.

Jenkins, J., Deuss, A., and Cottaar, S., Converted phases from sharp 1000 km depth mid-mantle heterogeneity beneath Western Europe, *Earth Planet. Sci. Lett.*, 459, 196–207, https://doi.org/10.1016/j.epsl.2016.11.031, 2017.

Kaneshima, S., Seismic scatterers at the shallowest lower mantle beneath subducted slabs, *Earth Planet. Sci. Lett.*, 286, 1–2, 304–315, https://doi.org/https://doi.org/10.1016/j.epsl.2009.06.044, 2009.

Kaneshima, S., Seismic scatterers in the mid lower mantle, *Phys. Earth Planet. Int.*, 257, 104–114, https://doi.org/https://doi.org/10.1016/j.pepi.2016.05.004, 2016.

Kaneshima, S. Seismic scatterers in the mid-lower mantle beneath Tonga-Fiji, *Phys. Earth Planet. Int.*, 274, 1–13. https://doi.org/https://doi.org/10.1016/j.pepi.2017.09.007, 2018.

Kaneshima, S., 2019. Seismic scatterers in the lower mantle near subduction zones. Geophys. J. Int. 219, S2–S20. https://doi.org/10.1093/gji/ggz241.

Kaneshima, S., Helffrich, G., 1998. Detection of lower mantle scatterers northeast of the Marianna subduction zone using short-period array data. J. Geophys. Res. 103, 4825–4838.

Kaneshima, S., Helffrich, G., 1999. Dipping low-velocity layer in the mid-lower mantle: evidence for geochemical heterogeneity. Science 283, 1888–1891.

Kaneshima, S., Helffrich, G., 2009. Lower mantle scattering profiles and fabric below Pacific subduction zones. Earth Planet. Sci. Lett. 282, 234–239.

Kaneshima, S., Helffrich, G., 2010. Small scale heterogeneity in the mid-lower mantle beneath the circum-Pacific area. Phys. Earth Planet. Inter. 183 (1–2), 91–103. https://doi.org/10.1016/j.pepi.2010.03.011.

Kennett, B.L.N., Engdahl, E.R., Buland, R., 1995. Constraints on seismic velocities in the earth from traveltimes. Geophys. J. Int. 122, 108–124.

Le Stunff, Y., Wicks Jr., C.W., Romanowicz, B., 1995. P'P' precursors under Africa: evidence for mid-mantle reflectors. Science 270 (5233), 74–77. https://doi.org/10.1126/science.270.5233.74.

Leng, K., Nissen-Meyer, T., van Driel, M., Hosseini, K., Al-Attar, D., AxiSEM3D: broadband seismic wavefields in 3-D global earth models with undulating discontinuities, *Geophysical Journal International*, 217 (3), 2125–2146, https://doi.org/https://doi.org/10.1093/gji/ggz092, 2019.

Mancinelli, N., and Shearer, P., Scattered energy from a rough core-mantle boundary modeled by a Monte Carlo seismic particle method: application to PKKP precursors, *Geophys. Res. Lett.*, 43, 7,963–7,972, doi:10.102/2016gl070286, 2016.

Margerin, L., Nolet, G., 2003. Multiple scattering of high-frequency seismic waves in the deep Earth: PKP precursor analysis and inversion for mantle granularity. J. Geophys. Res. 108, 2514. https://doi.org/10.1029/2003JB002455. B11.

Miller, M.S., Niu, F., 2008. Bulldozing the core-mantle boundary: localized seismic scatterers beneath the Caribbean Sea. Phys. Earth Planet. Inter. 170 (1–2), 89–94.

Nakagawa, T., Tackley, P., Deschamps, F., Connolly, J., 2012. Radial 1D seismic structures in the deep mantle in mantle convection simulations with self consistently calculated mineralogy. Geochem. Geophys. Geosyst. 13, Q11002. https://doi.org/10.1029/2012GC004325.

Neidell, N.S., Taner, M.T., 1971. Semblance and other coherency measures for multichannel data. Geophys. 36, 482–497.

Niu, F., 2014. Distinct compositional thin layers at mid-mantle depths beneath Northeast China revealed by the USArray. Earth Planet. Sci. Lett. 402, 305–312.

Niu, F., Kawakatsu, H., Fukao, Y., 2003. Seismic evidence for a chemical heterogeneity in the mid mantle: a slightly dipping and strong seismic reflector at mid-depth beneath the Mariana subduction zone. J. Geophys. Res. 108, B9. https://doi.org/10.1029/2002JB002384.

Revenaugh, J., Jordan, T.H., 1991. Mantle layering from ScS reverberations, 4, the lower mantle and core-mantle boundary. J. Geophys. Res. 96 (19), 811–19,824.

Rost, S., Thomas, C., 2009. Improving seismic resolution through array processing techniques. Surv. Geophys. 30, 271–299.

Rost, S., Garnero, E., Williams, Q., 2008. Seismic array detection of subducted oceanic crust in the lower mantle. *J. Geophys. Res*. 113 (B06303). https://doi.org/10.1029/2007JB005263.

Schumacher, L., Thomas, C., and Abreu, R., Out-of-plane seismic reflections beneath the Pacific and their geophysical implications, *J. Geophys. Res.*, 123, 2,286–2,302. https://doi.org/https://doi.org/10.1002/2017JB014728, 2018.

Shen, Y., Wolfe, C. J., and Solomon, S. C., Seismological evidence for a mid-mantle discontinuity beneath Hawaii and Iceland, *Earth Planet. Sci. Lett.*, 214 (1 − 2), 143–151, https://doi.org/https://doi.org/10.1016/S0012-821X(03)00349-2, 2003.

Stein, S., van der Lee, S., Jurdy, D., Stein, C., Wiens, D., Wysession, M., Revenaugh, J., Frederiksen, A., Darbyshire, F., Bollmann, T., Lodewyk, J., Wolin, E., Merino, M., Tekverk, K., 2011. Learning from failure: the SPREE mid-continent rift experiment. GSA Today 21 (9), 5–7.

Thomas, C., Kendall, J.-M., Helffrich, G., 2009. Probing two low velocity regions with PKP b-caustic amplitudes and scattering. Geophys. J. Int. 178, 503–512.

Vanacore, E., Niu, F., Kawakatsu, H., 2006. Observations of the mid-mantle discontinuity beneath Indonesia from S to P converted waveforms. Geophys. Res. Lett. 33https://doi.org/10.1029/2005GL025106. L04302.

Vanacore, E., Niu, F., Ma, Y., 2010. Large angle reflection from a dipping structure recorded as a PKIKP precursor: evidence for a low velocity zone at the core-mantle boundary beneath the Gulf of Mexico. Earth Planet. Sci. Lett. 293, 54–62.

Waszek, L., Schmerr, N.C., Ballmer, M.D., 2018. Global observations of reflectors in the mid-mantle with implications for mantle structure and dynamics. Nat. Commun. 9, 385. https://doi.org/10.1038/s41467-017-02709-4.

Wen, L., Helmberger, D.V., 1998. Ultra-low velocity zones near the core-mantle boundary from broadband PKP precursors. Science 279, 1701–1703.